

# Investigating nucleation of phase transitions in rod-coil block copolymers

Jingyu Shao, Yuliang Yang, Ping Tang\*

State Key Laboratory of Molecular Engineering of Polymers, Department of Macromolecular Science, Fudan University, Shanghai, 200433, China



## ARTICLE INFO

### Keywords:

Nucleation transitions  
Liquid crystal polymer  
Selfconsistent field theory

## ABSTRACT

It is known that the nucleation of liquid crystal polymers with orientation interactions can reduce the energy barrier during the polymer crystallization. In this work, we combine the SCFT and string method to explore the nucleation and liquid crystal behavior of rod-coil block copolymers. By examining nucleation transitions from cylinders with different directions to lamellae, we obtain the information of critical nuclei for the first time, including the volume, shape and energy barrier. We further investigate the impacts of orientation interactions along different transition paths. The results show that if the cylinder and lamellae have inconsistent directions, the nucleation will occur with relatively longer transition path and multiple reorientations, and thus leading to higher energy barrier. Nucleation under different Flory-Huggins interactions and nucleation via precursory metastable structures are investigated, and compared with the classical nucleation theory. This work develops the nucleation studies for complex block copolymers with segment orientations, which is helpful for understanding the nucleation of liquid crystal polymers.

## 1. Introduction

Nucleation, the starting point of a phase transition, plays a decisive role in determining the final structures and expected performances [1, 2]. It can be found in natural events such as steam condensation, water freezing, and mineral formation, but also in metal solidification, protein crystallization, food processing et al. [3,4] Among them, the information of the critical nucleus is of pivotal importance, including the energy barrier, shape, size and structure. According to the classic nucleation theory (CNT) [5–8], a nucleus grows to a new phase preferentially when the size beyond the critical nucleus or energy fluctuations exceed the nucleation energy barrier.

Block copolymers have attracted extensive interests due to their microphase separated structure and resulting excellent material properties [9–14]. However, owing to the complex processing conditions and long-chain nature, it is hard to reach their thermodynamic equilibrium state in experiments [15]. The expected performances of block copolymer materials are affected by non-equilibrium states reported in previous experiments [16–18]. On the account of metastable mesophases of block copolymers trapped in the nucleation transition, recognizing the significance of the nucleation in block copolymers will provide terrific opportunities to construct desired structures and properties of final materials [19–21]. However, it is still a challenging task to have an accurate description of the block copolymer critical nucleus. Although

advanced experimental characterization techniques added, the size observed usually exceeds critical nucleus size. In recent years, with the development of computational materials science and numerical simulation methods, significant progress has been made in the study of block copolymer nucleation. Applied approaches range from molecular dynamics [22], Monte Carlo simulation [23], and self-consistent field theory (SCFT) [24]. The well-established theoretical framework of SCFT has been proven to be effective in dealing with polymer nucleation. Cheng et al. [25] combined SCFT and the string method to simulate the nucleation of coil-coil block copolymers. They obtained detailed information of critical nuclei from the nucleation transition path and revealed the evolution process from a metastable phase to a stable ordered phase. Their work also concluded that the transition from lamellae to double gyroid follows a two-step nucleation process. Using the same method, our previous study found the epitaxial growth relationship between gyroid and lamellae through calculating nucleation transitions from arbitrary oriented lamellae to gyroid [26]. Although extensive researchers have made profound studies, to the best of our knowledge, none have been able to study the nucleation of block copolymers with rigid segments like liquid crystal structure. In fact, crystallization process of polymers is considered as a nucleation transition from the melt to liquid crystal first and further to the final crystal rather than directly from the melt to crystal. The liquid crystal mesophase, composed of ordered orientational stems, can reduce the nucleation energy barrier

\* Corresponding author.

E-mail address: [pingtang@fudan.edu.cn](mailto:pingtang@fudan.edu.cn) (P. Tang).

[27–29]. However, huge calculation size is required to guarantee the accuracy of the critical nucleus calculation, and the liquid crystal structure introduces the orientation variable and geometrical asymmetry of rods comparing to the Gaussian chain [30], which leads to an exponential increase in complexity and computing costs. These challenges have made researches on the nucleation of liquid crystal polymers undeveloped to date.

Many studies sought to uncover the mechanism of nucleation transition by proposing simple models [27,31–33]. The CNT is the most common theoretical model used to understand nucleation from the point of thermodynamics, which can date back to the 1870s when Gibbs performed the analysis of droplet formation in supersaturated water vapor [5,6]. The nucleation driving force is the free energy difference between phase transition states, and the competition between it and the interface energy determines whether the nucleus grows or shrinks. Recently, Bai et al. [34] used indirect methods by fixed-size nanoparticles to detect the critical ice nucleus, and have confirmed the effectiveness of CNT in describing the critical nucleus characteristics at the atomic scale. The results deepened the micro-mechanism understanding of nucleation transition. For polymer nucleation, the existence of the anisotropic nature and more than one length scale make the issue more complicated. Wickham et al. [35] investigated the nucleation transition from lamellae to cylinders for coil-coil block copolymers using the single-mode approximation to the Brazovskii model. They obtained an analytic expression for the interface free energy and the nucleus shape for the first time, and made quantitative predictions based on CNT. However, due to the complex structure of liquid crystal polymers, there is no suitable method to describe the nucleation process now.

In order to study the nucleation transition of liquid crystal polymer, we introduce the string method to SCFT for examining the nucleation transition of rod-coil block copolymers. We focus on the nucleation transition from the cylinder to lamellae and obtain its critical nuclei information for the first time, including volume, shape and energy barrier that contains nucleation driving force and interface energy based on CNT. Impacts of orientation interactions along different nucleation transition paths are systematically presented. In particular, we study nucleation under different Flory-Huggins interactions and nucleation via a metastable phase. The simulation results match with the CNT, which proves to be effective in describing the rod-coil block copolymer nucleation processes. Without the need for prior knowledge of the detailed pathway of nucleation, this work provides a method for prediction of the critical nuclei information and the nucleation process with segment orientations.

## 2. Theory and computation methods

**Self-consistent field theory (SCFT):** The detailed derivation of rod-coil model based on SCFT was first proposed by Pryamitsyn and Ganesan [36], here we only show a brief description with some parameters used. Consider an incompressible model system consisting of  $n$  rod-coil diblock copolymer chains within volume  $V$ . Each chain contains  $N_R$  rod segments and  $N_C$  coil segments, and the total chain length  $N = N_C + N_R$ . Assuming that the rod and coil segments have the same bulk number density  $\rho_0 = nN/V$ , then the volume fractions for coil and rod blocks can be obtained as  $f_C = N_C/N$  and  $f_R = N_R/N = 1 - f_C$  respectively.  $\beta$  is introduced to represent the geometrical asymmetry between coils and rods, defined as  $\beta = bN/a\sqrt{(N/6)}$ , where  $a$  and  $b$  are statistical segment length of rods and coils, respectively. As  $\beta$  increases, the rods become slender. The coil is modeled as a Gaussian chain and the stiffer block is modeled as a rod of finite thickness with a unit orientation  $\mathbf{u}$ . The rods cannot be bent, having infinite bending energy. The system free energy is described as follows, and we note that all the energy in the system is in the unit of  $nk_B T$ .

$$F = \frac{1}{V} \int_V d\mathbf{r} \left\{ \chi N \varphi_C(\mathbf{r}) \varphi_R(\mathbf{r}) - \omega_C(\mathbf{r}) \varphi_C(\mathbf{r}) - \omega_R(\mathbf{r}) \varphi_R(\mathbf{r}) - \eta(\mathbf{r}) [1 - \varphi_C(\mathbf{r}) - \varphi_R(\mathbf{r})] - \frac{\mu N}{2} \mathbf{T}(\mathbf{r}) : \mathbf{T}(\mathbf{r}) + \mathbf{M}(\mathbf{r}) : \mathbf{T}(\mathbf{r}) \right\} - \ln Q \quad (1)$$

where  $\chi$  is Flory-Huggins interaction parameter between the rod block and coil block.  $\mu N$  is Maier-Saupe orientation interaction parameters.  $\varphi_C(\mathbf{r})$  and  $\varphi_R(\mathbf{r})$  are the local density distributions of coil and rod blocks,  $\omega_C(\mathbf{r})$  and  $\omega_R(\mathbf{r})$  are corresponding mean fields,  $\eta(\mathbf{r})$  is the potential field that guarantees the incompressibility condition,  $\mathbf{T}(\mathbf{r})$  is the orientation order parameter, and it is defined by  $\mathbf{T}(\mathbf{r}) = \frac{1}{Q} \int_0^{1-f} ds \int d\mathbf{u} q_C(\mathbf{r} - \beta s\mathbf{u}, f) \exp[-\int_0^{1-f} ds \Gamma(\mathbf{r} - \beta s\mathbf{u} + \beta s\dot{\mathbf{u}}, \mathbf{u})] (\mathbf{uu} - \frac{1}{3})$ . The orientation field  $\mathbf{M}(\mathbf{r})$  is conjugated with the order parameters, namely,  $\mathbf{M}(\mathbf{r}) = \mu N \mathbf{T}(\mathbf{r})$ .  $Q$  is the single-chain partition function:

$$Q = \frac{1}{V \int d\mathbf{u}} \int d\mathbf{u} \int d\mathbf{r} \exp \left[ - \int_0^{1-f_C} ds \Gamma(\mathbf{r} + \beta s\mathbf{u}, \mathbf{u}) \right] q_C(\mathbf{r}, f_C) \quad (2)$$

where  $\Gamma(\mathbf{r}, \mathbf{u})$  is the combination of the density field and the orientation field, which is defined as  $\Gamma(\mathbf{r}, \mathbf{u}) \equiv \omega_R(\mathbf{r}) - \mathbf{M}(\mathbf{r}) : (\mathbf{uu} - \mathbf{I}/3)$ ,  $\mathbf{I}$  is a  $3 \times 3$  unit matrix, and  $\mathbf{u}$  is unit orientation vector discretized into icosahedron triangular meshes in a spherical surface, as described in our previous paper [37].  $q_C(\mathbf{r}, f)$  represents the probability of finding a coil segment  $s$  ( $0 < s \leq f_C$ ) at the position of  $\mathbf{r}$ . Exponential term shows the probability that the rods have an angle  $\mathbf{u}$  with the link between the coil and rod block at the position of  $\mathbf{r}$ . It satisfies a modified diffusion equation based on the Gaussian chain with the initial value  $q_C(\mathbf{r}, 0) = 1$ .

According to the saddle point approximation [38], minimize the free energy functional with respect to each field and we can get a set of self-consistent equations. The modified diffusion equation can be efficiently solved by pseudospectral method proposed by Tzeremes et al. [39]. The rod block concentration and orientation order parameter are calculated in the Fourier space using the fast Fourier transform [40]. The SCFT equations can only be numerically solved, refer to our previous publications [30,41,42], and the final stable phase structure is thus determined as the one having the lowest free energy.

**String method:** The string method is first proposed by E, Ren and Vanden-Eijnden [43–45], and is convenient to find a minimum energy path (MEP) on the energy landscape connecting two states. Once the stable phase structure is determined by SCFT, the next step is to use it as input for initializing the string. We here briefly show the key steps in the string method, and the detailed information refers to our previous paper [26,46]. Consider a string  $\psi(\alpha)$ , where each point on it corresponds to a state with specific phase structure, including morphologies (density order parameters) and free energy. The two ends are denoted by order parameters as  $\psi(0) = \kappa_S(\mathbf{r})$  and  $\psi(1) = \kappa_E(\mathbf{r})$ , where  $\mathbf{r}$  is the position vector. The initial nuclei  $S_\alpha$  along abscissa of the string  $\alpha \in (0, 1)$  are generated with its sphere radius  $R(\alpha)$  varying linearly from 0 to  $L/2$ , and a series of initial states  $\psi(\alpha)$  are defined as

$$\psi(\alpha) = \kappa_\alpha(\mathbf{r}) = \begin{cases} \kappa_E(\mathbf{r}), & \text{if } \mathbf{r} \in S_\alpha \\ \kappa_S(\mathbf{r}), & \text{if } \mathbf{r} \notin S_\alpha \end{cases} \quad (3)$$

where the  $L$  is the side length of the calculation box. In our subsequent calculations, only the data with nucleus volume fraction not exceeding 0.5 is kept, which guarantees that the nucleus is not influenced by the geometrical constraint. In addition to the nucleation energy barrier, we also want to study the structure, shape and size of the critical nucleus. Thus, the boundary of the nucleus needs to be defined. For the case of order-disorder transition, the nuclear boundary is obtained directly, but for the order-order transition, another definition is needed. Here we use the method proposed by Lin et al. [47] to define a point-wise stable-phase-density function.

$$\Psi(\mathbf{r}) \equiv \frac{|\kappa_a - \kappa_s|(\mathbf{r})}{|\kappa_a - \kappa_s|(\mathbf{r}) + |\kappa_a - \kappa_e|(\mathbf{r})} \quad (4)$$

$$|\kappa_a - \kappa_b|(\mathbf{r}) \equiv \int d\mathbf{r}' K(\mathbf{r}' - \mathbf{r}) [\kappa_a(\mathbf{r}') - \kappa_b(\mathbf{r}')]^2 \quad (5)$$

where the weight function  $K(\mathbf{r}' - \mathbf{r})$  is a mollifier to make the  $\Psi(\mathbf{r})$  smoother, and has the form of Gaussian distribution as follows:

$$K(\mathbf{r}' - \mathbf{r}) = \exp\left(-\frac{|\mathbf{r}' - \mathbf{r}|}{2\gamma^2}\right) \quad (6)$$

where the adjustment parameter  $\gamma$  is set to balance the accuracy and smoothness of nuclear boundaries, which can be obtained by setting a threshold on  $\Psi(\mathbf{r}) = 0.5$  in this work. Furthermore, the string in this work is discretized into 20 or 40 points, each of which is carried out to a convergence of at least  $10^{-5}$  in free energy and  $10^{-4}$  in fields values.

### 3. Results and discussion

Numerous studies have focused on the phase transition pathways of polymers, which found that the matching dominant reciprocal lattice vectors and unit cell sizes are two crucial factors [26,48–51]. If the both two factors mismatch, the nucleation transition may not occur due to the high energy barrier or large polymer chains transport. Each self-assembled structure in block copolymers belongs to a specific space

group, and different structures may have a same space group, which are distinguished by the strongest modulation of different reciprocal lattice vectors [48]. Here, we denote the reciprocal lattice vectors of the cylinder and lamellae by crystallographic direction and crystallographic plane group in real space, respectively, which are represented by Miller indices [52]. Each crystallographic plane and crystallographic direction group contains various planes or directions: the  $\langle 111 \rangle$  crystallographic direction group contains eight different directions like  $[111]$ ,  $[\bar{1}11]$ ,  $[1\bar{1}\bar{1}]$  and  $[\bar{1}\bar{1}1]$ , etc. Due to the periodicity, they can be divided into four different directions. However, our target phase structure (101) lamellae have the symmetry along the  $x$ - $z$  plane, the cylinders whose directions are symmetric about the  $x$ - $z$  plane will have the same nucleation pathways. As a result, there are only two essentially different nucleation pathways, which are shown by cylindrical  $[111]$  and  $[\bar{1}11]$  in our paper.

Fig. 1a shows two ends of the string for investigating the nucleation transition. We determine the optimized cell size of the block copolymer in unit of the radius of gyration  $R_g$  by minimizing the free energy with respect to the cubic box size  $D$ . Different  $\chi N$  values correspond to different optimal cell sizes, which become small with increased  $\chi N$ . We construct them through the strong segregation boundary [53], and Table 1 indicates an example under parameters of  $f_c = 0.7$ ,  $\chi N = 19$ ,  $\mu N = 10$  and  $\beta = 2$ . However, the existence of the rod in rod-coil model makes the arrangement and assembly of blocks frustrated. Therefore, the optimal cell sizes of the  $\langle 111 \rangle$  cylinders and  $\{101\}$  lamellae are not

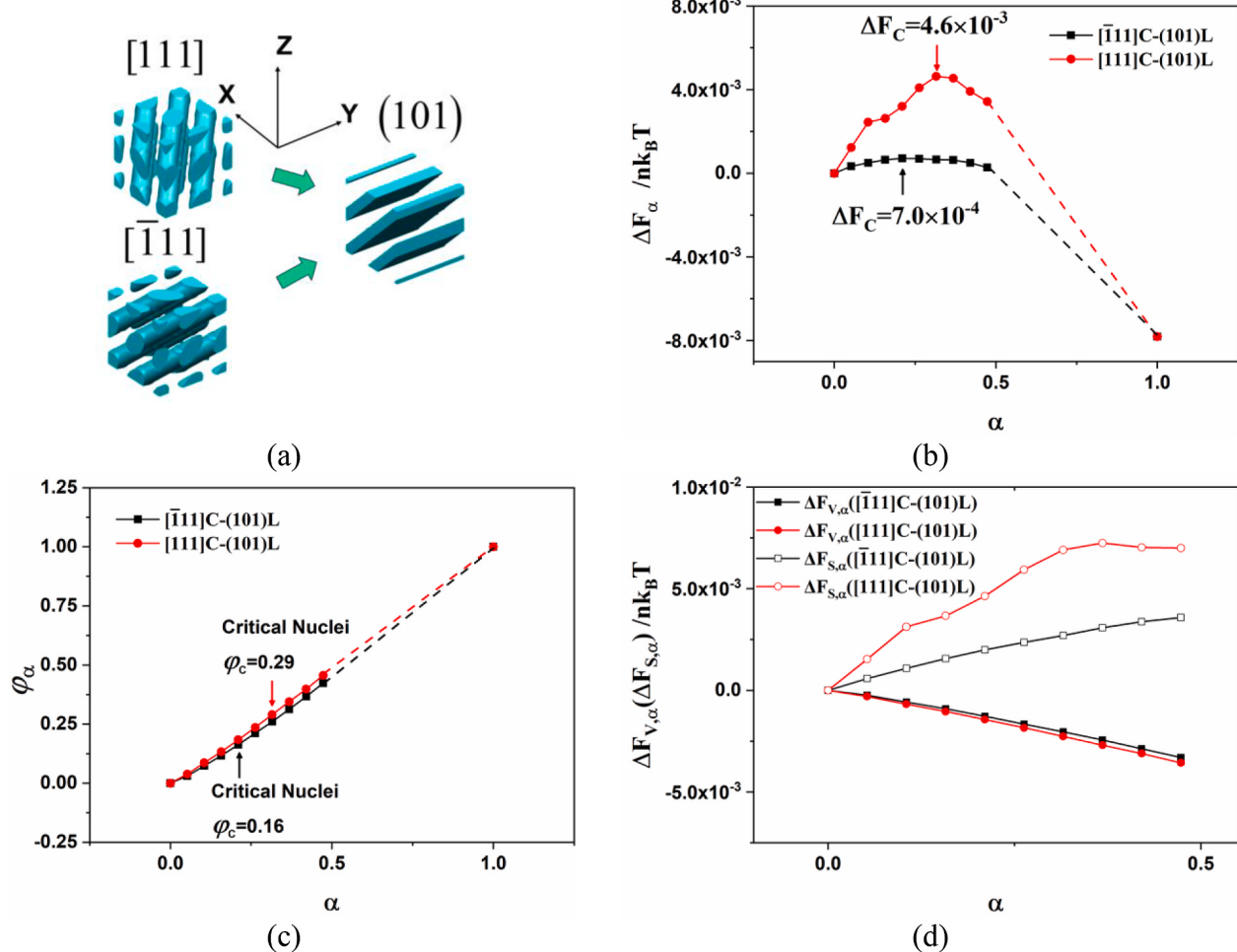


**Fig. 1.** Nucleation transitions of rod-coil block copolymers. (a) Cylinders or lamellae (only show rods for clarity) of the two string ends. (b) Energy barrier of single chain as a function of string  $\alpha$  (MEPs) between  $[111]$ ,  $[\bar{1}11]$  cylinders and  $(101)$  lamellae. (c) Changes of nucleus volume during the nucleation. (d) Changes of the nucleation driving force  $\Delta F_{v,\alpha}$  and interface energy  $\Delta F_{s,\alpha}$  during the nucleation.

**Table 1**Basic Parameters Setting in the Nucleation Transition under parameters of  $f_C = 0.7$ ,  $\chi N = 19$ ,  $\mu N = 10$  and  $\beta = 2$ 

phases	optimal cell size( $D_x, D_y, D_z$ ) ( $R_g$ )	calculation size ( $L_x, L_y, L_z$ ) ( $R_g$ )	discretization step( $R_g$ )
[111] cylinder	(3.77, 3.77, 3.77)	(22.62, 22.62, 22.62)	(0.1767, 0.1767, 0.1767)
[111] cylinder	(3.77, 3.77, 3.77)	(22.62, 22.62, 22.62)	(0.1767, 0.1767, 0.1767)
(101) lamellae	(4.12, 4.12, 4.12)	(24.72, 24.72, 24.72)	(0.1931, 0.1931, 0.1931)

exactly same, but the difference between them is less than 9%, which can be ignored in our calculations. The critical nucleus grows from initial cylinders and its calculation presents a computational challenge to guarantee the accuracy. For example, due to the limitation of calculation costs, the calculation size cannot be infinite, and the boundary must be specified. This truncation will result in numerical errors when the critical nucleus approaches the calculational boundaries, but errors are negligible when the critical nucleus stays well away from the boundaries. In a word, the huge calculation size is required to guarantee the accuracy of the critical nucleus calculation, but it also requires finer spatial resolution and thus reduces the computational efficiency. Without losing the key information of critical nuclei, the calculation sizes of initial cylinders and lamellae are chosen to be 6 times the corresponding optimal cell size along each axis, and that of the intermediate states during the nucleation transition varies linearly between the two ends of string for calculation stability. In all subsequent calculations, we set the number of lattice points in the simulation as  $128 \times 128 \times 128$  with the discretization step of about  $0.2 R_g$ .

To explore the nucleation transitions with different initial cylinders, we calculate MEPs of nucleation transitions from [111],  $[\bar{1}11]$  cylinders to (101) lamellae, as shown in Fig. 1b, and the entire string is discretized into 20 states. For focusing on the nucleation phenomenon, the calculated parameters should locate in the region of binodal transition, near which is the cylinder-lamellar phase boundary. So, we select the nucleation transition parameters near the phase transition point with  $f_C = 0.7$ ,  $\chi N = 19$ ,  $\mu N = 10$  and  $\beta = 2$ . The critical nucleus of (101) lamellae can be obtained when the energy barrier reaches its maximum. The nucleation energy barrier is expressed as  $\Delta F_C = F_C - F_0$  in the unit of  $n k_B T$ , where  $F_C$  and  $F_0$  are free energies of the critical ( $\alpha = C$ ) and initial states ( $\alpha = 0$ ), which can be calculated by Eq. (1). Fig. 1b shows that the nucleation energy barrier relates to the direction of initial cylinders. The nucleation energy barrier from [111] cylinder to (101) lamellae is 6.42 times that from  $[\bar{1}11]$  cylinder although [111] and  $[\bar{1}11]$  cylinders have same free energy. We note that the later part of nucleation will become inaccurate when the nucleus extends near to the calculation domain boundary (the nucleus volume fraction exceeds 0.5), and we drop out these data and replace them with dashed lines in Fig. 1b–c.

On the basis of the CNT from a thermodynamic viewpoint, the formation of a critical nucleus depends on the nucleation driving force and interface energy. As the coexistence of a part of the old phase (cylinder) with the nucleus of new phase (lamellae), the difference in bulk free energies between lamellae and cylinder phase brings the nucleation driving force and the formation of an interface between the cylinder and the nucleus leads to the interface energy. When the nucleation from the old phase completely evolves to a new phase, the interface disappears, and the nucleation driving force  $\Delta F_{V,1}$  equals to  $\Delta F_1 = F_1 - F_0$ , where  $F_0$  and  $F_1$  are free energies of the initial ( $\alpha = 0$ ) and final ( $\alpha = 1$ ) states during the nucleation transition, respectively. Thus, the unit volume of nucleation driving force can be obtained as  $\Delta F_{V,1}/V$ , obviously, not dependent on the nucleation path, where  $V$  represents the total volume of calculation box,  $V = L^3$ . Then, a simple expression for nucleation driving force along the nucleation path can be derived as  $\Delta F_{V,\alpha} = V_\alpha (\Delta F_{V,1} / V) = \Delta F_1 \phi_\alpha$ , where  $V_\alpha$  is the nucleus volume along the string and  $\phi_\alpha = V_\alpha / V$  is the nucleus volume fraction. Fig. 1c shows the  $\phi_\alpha$  as a function of the nucleation path  $\alpha$ . The corresponding interface energy is thus expressed as the subtraction of nucleation driving force from the

energy barrier based on CNT,  $\Delta F_{S,\alpha} = \Delta F_\alpha - \Delta F_{V,\alpha}$ , where  $\Delta F_\alpha$  is the energy barrier during the nucleation process,  $\Delta F_\alpha = F_\alpha - F_0$ . Obviously, we can calculate the nucleation driving force and interface energy provided that the volume of nucleus is obtained. Fig. 1d presents the calculated nucleation driving force and interface energy during the nucleation transition. From Fig. 1c, the changes of nucleus volume fractions  $\phi_\alpha$  during two nucleation transitions are different, the  $\phi_\alpha$  in the transition from the initial cylinder with [111] direction is always bigger than that with  $[\bar{1}11]$  cylinder. The volume fraction of the former critical nucleus is 0.29, which is about 1.8 times that of latter (0.16). Obviously, the nucleation driving force is proportional to  $\phi_\alpha$  as mentioned above. However,  $\Delta F_1$  is invariant for the two nucleation transitions, and the ratio of the critical nucleation driving forces is same as the ratio of critical nucleus volume fractions, that is, 1.8 between the two nucleation transitions. At the same time, the interface energy of the former transition is significantly large, which leads to higher nucleation energy barrier, as shown in Fig. 1d–b.

The detailed morphology of the critical nucleus is illustrated in Fig. 2. From Fig. 2a–b, we found that critical nuclei of the two nucleation transitions locate at the centre of corresponding morphologies, and the rest of morphologies remain as the corresponding initial cylinder phase. Fig. 2c–d are amplitudes of the Fourier transformation of the 3D density profile for rods, which are proportional to the experimental scattering intensity. We spherically average the scattering peaks to mainly clearly demonstrate the structure of the critical nucleus during the transition from lamellae to cylinders. As shown in Fig. 2c–d, it is obvious that the scattering reflections is consistent with the scattering signature for hexagonal packing cylinders. The primary peak  $q^*$  gives higher order reflections at  $\sqrt{3}q^*$ ,  $2q^*$  and  $\sqrt{7}q^*$ . At the same time, it also shows scattering of a lamellar morphology, where higher-order reflections are identified as multiples of the primary scattering peak ( $q^*$ ,  $2q^*$  and  $3q^*$ ). Fig. 2e–f shows the order parameters of  $\varphi_C$ ,  $\varphi_R$ ,  $\Psi$  profiles of the (010) cross section, whose definition has been introduced in the section of theory and computation methods. We can quantitatively conclude that the point-wise stable-phase-density function  $\Psi$  is highest in the centre of the critical morphologies and decreases sharply beyond a certain distance, which allows the boundary of the critical nucleus to be determined clearly. However, both  $\Psi$  in the two critical morphologies have some fluctuations, which is higher in the latter transition, representing the uneven shape of nucleus. The trend of order parameter  $\varphi_C$  or  $\varphi_R$  shows a particular structure, which is same inside the two critical nuclei.

To view a more detailed microscopic morphology, we draw the critical nuclei with their internal structures alone, as shown in Fig. 2g–h, where the cyan and red colors represent the rods distribution and the boundary of the nucleus, respectively. The critical nuclei both have lamellar structures inside, which confirms the results obtained from the above spectrum analysis and order parameters profiles, indicating the evolution from cylinders to lamellae. Furthermore, the surface of the critical nucleus is rough during the transition from [111] cylinder to (101) lamellae, which explains the reason for higher interface energy and more fluctuations in  $\Psi$ . To compensate for this higher interface energy, the nucleation transition requires a greater nucleation driving force with a bigger critical nucleus volume. However, the nucleation energy barrier for this transition is still much higher than that from  $[\bar{1}11]$  cylinder to (101) lamellae, as indicated in Fig. 1b–d.

The shapes and the free energy barriers of critical nuclei are both different in the two nucleation transformations. We suppose this may be

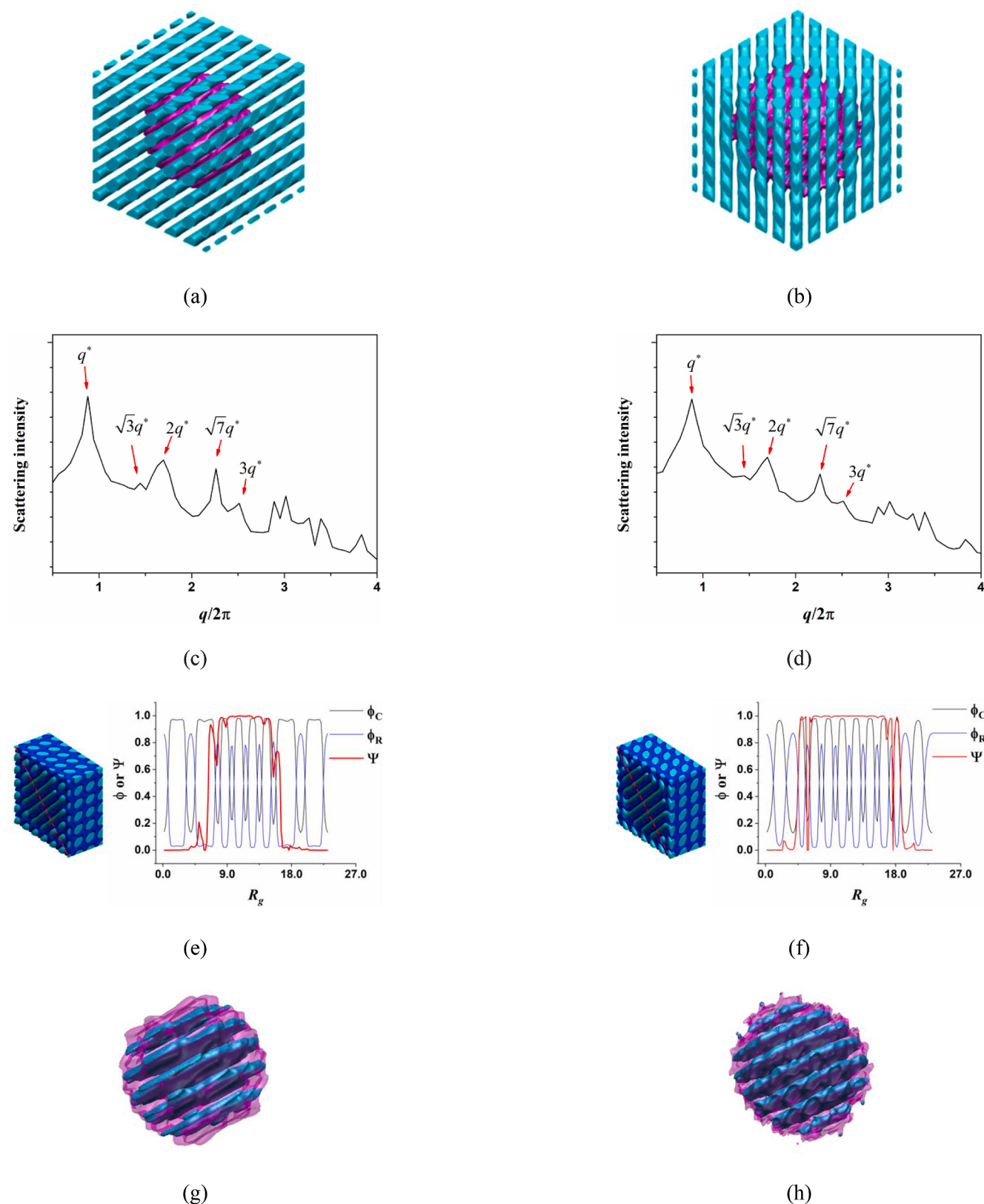


**Fig. 2.** Critical nuclear structures of rod-coil block copolymers. (a) and (b) are critical states. (c) and (d) are corresponding spectrum analysis simulated from morphologies by our SCFT calculations. (e) and (f) represent order parameters profile of the (010) cross section along the red dotted line in the two critical states. (g) and (h) show the nuclei and their internal structures for clarity. The cyan, blue and red colors in morphologies indicate the rods, coils distribution and the boundary of the nucleus. The left and right columns represent for the nucleation from  $\bar{[1}11]$ , and  $[111]$  cylinder to  $(101)$  lamellae, respectively. (For interpretation of the references to color in this figure legend, the reader is referred to the Web version of this article.)

related to the overall transition pathway and orientation interactions. To examine the first factor, we calculate the corresponding two spinodal phase transition pathways. A different initialization method is needed that order parameters of the state on the string evolve simultaneously in all calculation space [46,54]. In this case, each valley on the MEP corresponds to a metastable structure, and the entire string is discretized into 40 states. As shown in Fig. 3a, during the transition from [111] cylinder to (101) lamellae, three free energy barriers and two metastable phases exist, suggesting three phase transitions are experienced. In particular, (011) perforated lamellae first forms as a metastable phase ( $\alpha = 0.28$ ), and then it further experiences a six-branch network structure for reorientation transition to (101) perforated lamellae ( $\alpha = 0.77$ ), after which the target lamellar phase is formed. However, due to the lower energy barrier of cylinders and perforated lamellae, it is possible to have a reversible phase transition, which is also the reason for often observing perforated lamellae in experiments. Therefore, some additional means, such as magnetic field [55], are needed to guarantee the direction of the phase transition in experiments. In contrast, the transition from initial cylinder with [111] direction, as shown in Fig. 3b, only undergoes two phase transitions. Specifically, [111] cylinder nucleates to the metastable (101) perforated lamellae ( $\alpha = 0.54$ ) first, and then to the target lamellae. Of course, the nucleation transition has longer transition path with [111] initial cylinder, meaning large polymer chains transport. At the same time, the two transitions also have higher free energy barriers using this initialization method, which are in mutual agreement with Fig. 1b.

Experiments have shown that reorientation mostly occurs during nucleation and growth of the rod-coil block copolymers [55]. To examine the second factor, we consider the changes of average orientation degree and average orientation interaction energy during the transition. The order parameter  $\bar{T}_\alpha(\mathbf{r}) = 3/2\lambda_\alpha(\mathbf{r})$  can be used to represent the orientation degree of rods [36], where  $\lambda_\alpha(\mathbf{r})$  is the maximum eigenvalue of the orientation tensor  $\mathbf{T}_\alpha(\mathbf{r})$ . The average orientation degree of the nuclei is thus given as:  $M_\alpha = \int \bar{T}_\alpha(\mathbf{r}) dV_\alpha / V_\alpha$ . Fig. 4a shows the change of the average orientation degree  $M_\alpha$  during nucleation transitions from [111], [111] direction cylinders to (101) lamellae. The average orientation degree decreases first and then increases during both two nucleation transitions, but it changes twice during the transition from the initial cylinder with [111] direction, in contrast, only once in the other transition. Combined with Fig. 3, the emergence of each metastable phase is accompanied with the fusion of independent phase regions, which leads to the reorientation of rod blocks. Different nucleation transitions will result in different changes of average orientation degree. After the reorientation of rod block, the critical nucleus occurs and the orientation between rods inside the nucleus will adjust

again to minimize the system free energy, accompanied with the increased average orientation degree. It is noted that the nucleation from [111] cylinder to (101) lamellae has a slightly lower minimum of average orientation degree. Due to the limitation of calculation conditions, the string representing the nucleation pathway cannot be discretized into more than 20 points, and that results in the minimum points in Fig. 4a are not necessarily the corresponding lowest points, especially in the nucleation from the initial cylinder with [111] direction because of its longer nucleation path. However, the results can still represent the reorientation process of rod blocks.

The average orientation degree only considers the change of maximum orientation direction, which can only reflect the reorientation process of rods during the nucleation. To find specific effect of average orientation degree on the nucleation energy barrier, we calculate the average orientation interaction energy in the nuclei, which has a similar definition as  $M_\alpha$ :  $f_\alpha^0 = \int F_\alpha^0(\mathbf{r}) dV_\alpha / V_\alpha$ , where  $F_\alpha^0(\mathbf{r})$  is orientation interaction energy calculated in the Maier-Saupe interaction form [56], namely,  $F_\alpha^0(\mathbf{r}) = (\mu N/2)\mathbf{T}(\mathbf{r}) : \mathbf{T}(\mathbf{r})$ . The change of average orientation interaction energy in the nuclei during nucleation transitions is shown in Fig. 4b. Although both nucleation transitions (from [111], [111] direction cylinders to (101) lamellae) have same parameters condition, the one which experiences more reorientations has lower average orientation interaction energy, resulting in a higher nucleation energy barrier. After the reorientation, the orientation interaction energy will increase to a certain degree, and thus the system free energy becomes lower, consistent with Fig. 4a. Moreover, the change of average orientation interaction energy also indicates the multi-step reorientations.

To give a more intuitive description for reorientation process of rods, we draw a two-dimensional distribution of the  $M_\alpha$  along (010) plane at the middle of the Y-axis direction, as shown in Fig. 4c-d. Rod blocks will be pre-oriented at the initial cylinder, and then reorient to the targeted orientation accompanied with the fusion between the independent phase regions, thus resulting in the critical nucleus formation. More concretely, during the nucleation transition from [111] cylinder to (101) lamellae, the reorientation will mainly occur in the (010) plane first, which can be seen from the deformation of initial cylinders, resulting in its first minimum point in Fig. 4a. Then rod blocks pre-orient along the (101) plane, which is the reason for the second minimum point, and in contrast, it is also the only reorientation process during the transition from the initial cylinder with [111] direction, leading to its only minimum point in the average orientation degree changes.

Although the initial cylinder phase structures belong to the same crystallographic direction group, the different directions of cylinders can lead to different nucleation transition paths. The [111] cylinder phase, which has a relatively closer direction to (101) lamellae,

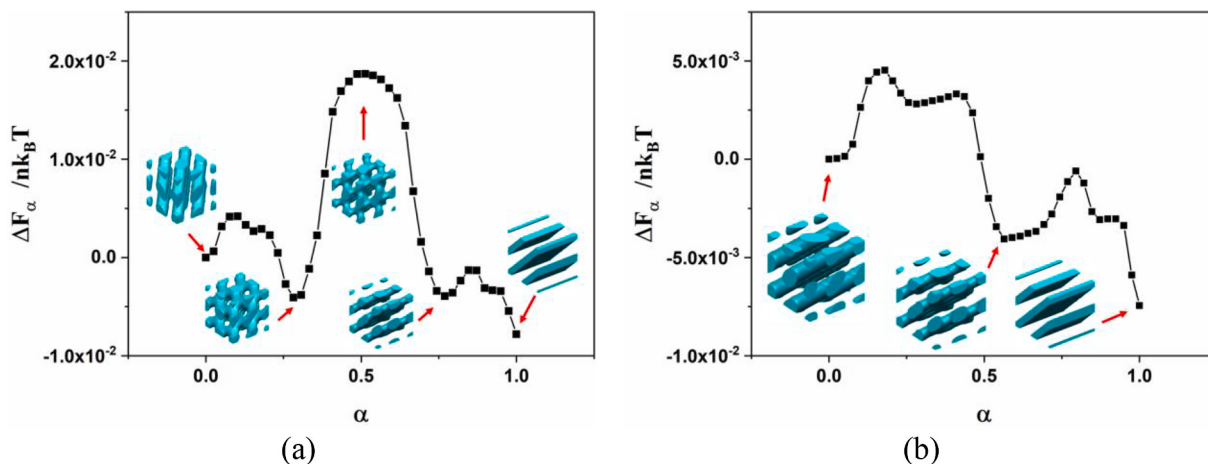


**Fig. 3.** The MEP calculated to observe the spinodal phase transition. (a) From [111] cylinder to (101) lamellae. (b) From [111] cylinder to (101) lamellae. The corresponding morphologies (only rods) on the string are presented with arrows.

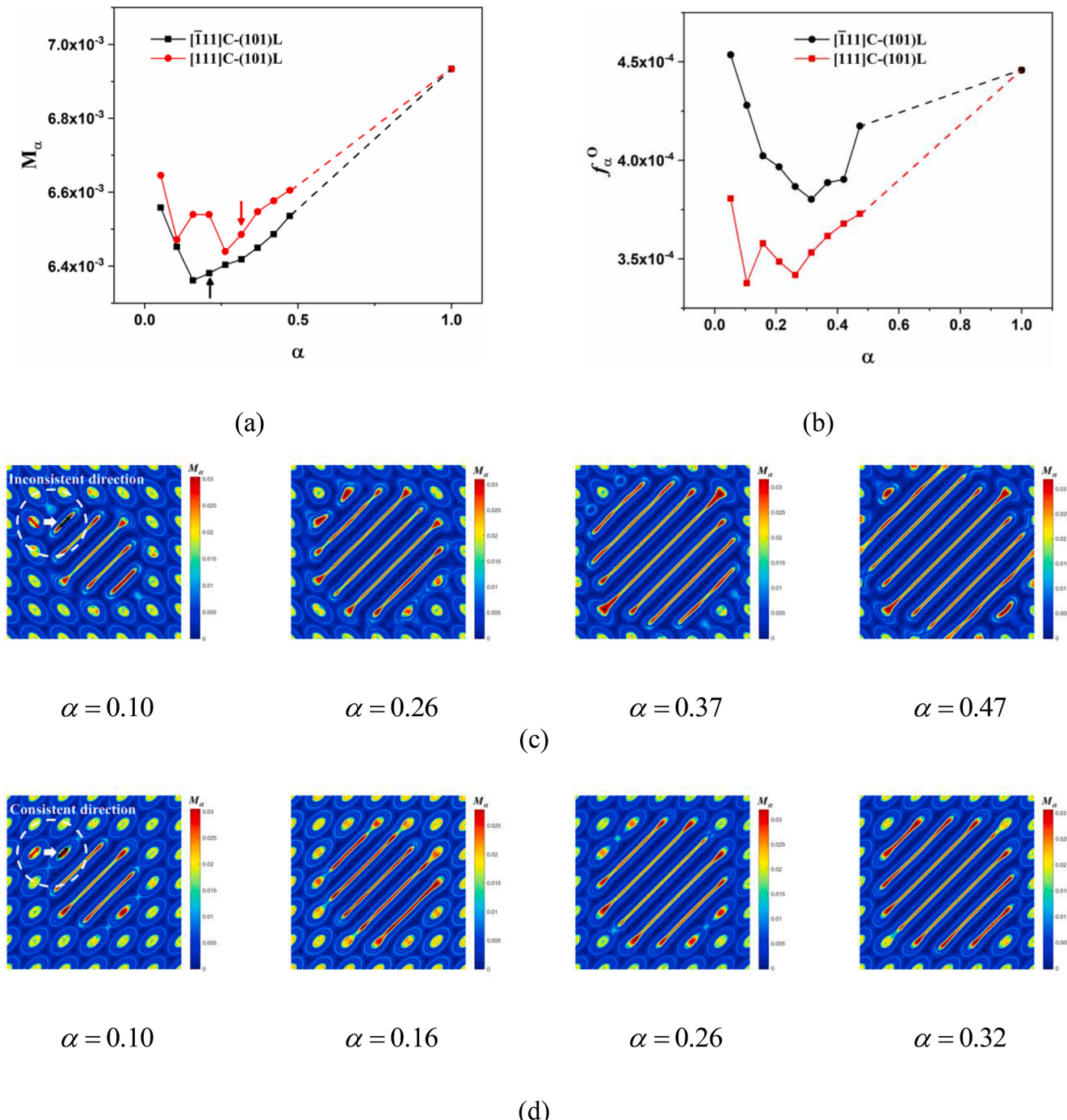


**Fig. 4.** Changes in orientation variable of rods in the nuclei during nucleation transitions. (a) Average orientation degree, where the positions indicated by the arrows are the critical nuclei. (b) Average orientation interaction energy. Two-dimensional distributions of the orientation degree along (010) plane at the middle of the Y-axis direction. (c) From  $[111]$  cylinder to  $(101)$  lamellae. (d) From  $[\bar{1}11]$  cylinder to  $(101)$  lamellae.

undergoes shorter nucleation path and fewer reorientations during the nucleation transition with a lower nucleation energy barrier. In contrast, inconsistent direction will lead to longer nucleation path and multi-step reorientations, resulting in a higher nucleation energy barrier.

To further understand the effect of the interaction between different species in the block copolymers on the nucleation transition, we calculate a series of nucleation transitions from  $[\bar{1}11]$  cylinders to  $(101)$  lamellae under different Flory-Huggins parameters  $\chi N$ . From Fig. 5a, as  $\chi N = 18.4$ , the free energy barrier per chain is  $0.0012 k_B T$ , which becomes lower with increased  $\chi N$ . Experiments have measured the Flory-Huggins interaction for the rod-coil block copolymer, and verified the

empirical form of  $\chi N c / T$  [57]. The results consistent with the Flory-Huggins theory [58], where  $c$  is a constant related to the interaction force between rod and coil blocks. Due to the rod blocks in our calculation have relatively lower orientation degree and orientation interaction energy as indicated in Fig. 4, we ignore the change of  $\mu$  with temperature and only focus on that of  $\chi$ . In this way, we can relate the supercooling degree as  $\Delta T = cN(1/\chi_m N - 1/\chi N)$ , where  $\chi_m N$  is the phase transition point between the cylinder and lamellae, which equals to 17.57 in our investigated parameters of  $f_C = 0.7$ ,  $\mu N = 10$  and  $\beta = 2$ . We calculate the changes of critical nucleus volume  $V_C$  with  $1/\Delta T^3$  and the nucleation energy barrier  $\Delta F_C$  with  $1/\Delta T^2$  in Fig. 5b, showing that

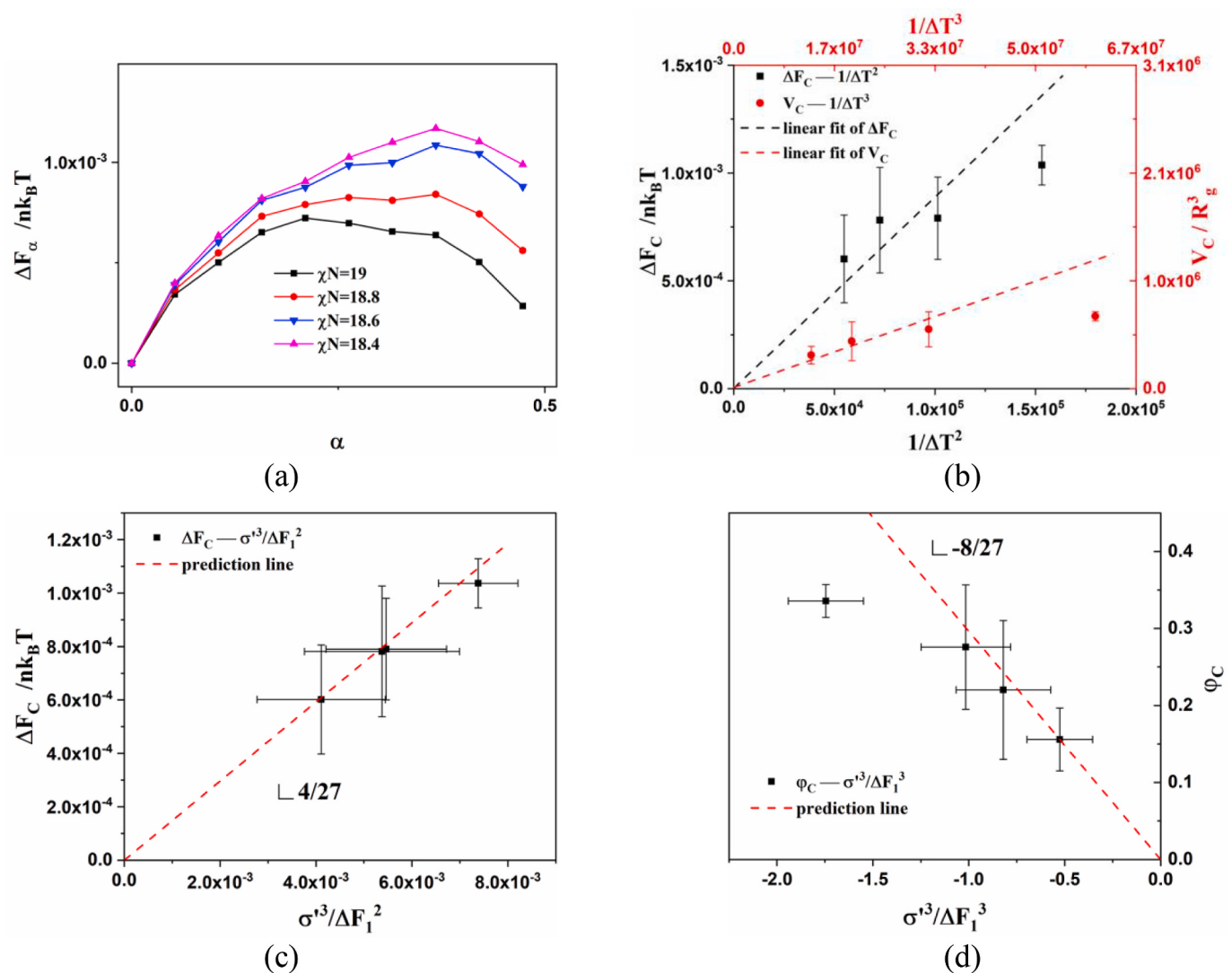


**Fig. 5.** The comparisons between the CNT prediction and SCFT simulation results. (a) MEP of nucleation transition from  $\bar{[111]}$  cylinder to (101) lamellae with  $\chi N$  from 18.4 to 19. (b) The nucleation energy barrier and critical nucleus volume change with supercooling. (c) The nucleation energy barrier changes with  $\sigma'^3 / \Delta F_1^2$ . (d) The critical volume fraction changes with  $\sigma'^3 / \Delta F_1^3$ . The error bar is calculated by standard deviation.

they both decrease with increasing the supercooling degree and have a proportional relationship with  $1/\Delta T^2$  or  $1/\Delta T^3$  in a certain range. This scaling relation is almost consistent with CNT. The error bar is calculated by the standard deviation, which is same as the subsequent discussions. Due to the complex copolymer structure with rigid blocks and orientation interactions, the assumptions we make have some deviations. Specifically,  $\chi$  and  $\mu$  both become small with decreased supercooling temperature, and thus the assumption of constant  $\mu$  makes the supercooling temperature calculated from the empirical form  $\Delta T = cN(1/\chi_m N - 1/\chi N)$  lower than the actual value. However,  $\chi$  plays a decisive role in determining nucleation energy barrier and critical nucleus volume under high supercooling temperature, where the deviation can be ignored. Moreover, lower supercooling temperature corresponds to a weak segregation, which will result in wider interface with the deviations of critical nucleus volume.

Fig. 5b shows that the nucleation energy barrier  $\Delta F_C$  vs.  $1/\Delta T^2$  and the critical nucleus volume  $V_C$  vs.  $1/\Delta T^3$  deviate a little from the CNT. Therefore, we consider a more suitable method according to the calculated nucleation information based on the SCFT and string method, to further compare with the CNT. In this work, we refer to  $\sigma$  as the “interface energy density”, that is, the unit area of interface energy

between the cylinder and the nucleus of (101) lamellae, which varies with  $\chi N$  in our model. Assume in a three-dimensional nucleation model, the interface between the nucleus and old phase is very sharp with a consistent shape during different nucleation transitions, and the critical nucleus always has same bulk structures as the ultimate object phase. The energy barrier changes during nucleation transition can be calculated as:

$$\Delta F(V_\alpha) = \phi_\alpha \Delta F_1 + \sigma' \phi_\alpha^{2/3} \quad (7)$$

where  $\sigma'$  is the modified unit area of interface energy  $\sigma' = (V \Delta F_C - V_C \Delta F_1) / (V^{2/3} L)$ . See Appendix for detailed derivation. In eq. (7), the first and second term in the right-hand side are nucleation driving force and interface energy, respectively. When the critical state is reached,  $\partial \Delta F / \partial \phi_\alpha = 0$ , and the critical nucleus volume fraction is derived as:

$$\phi_C = - \left( \frac{8}{27} \right) \frac{\sigma'^3}{\Delta F_1^3} \quad (8)$$

Substituting Eq. (8) into Eq. (7), the nucleation energy barrier in the unit of  $nk_B T$  is derived as:

$$\Delta F_C = \left( \frac{4}{27} \right) \frac{\sigma'^3}{\Delta F_1^2} \quad (9)$$

We plot the nucleation energy barrier  $\Delta F_C$  against  $\sigma'^3 / \Delta F_1^2$  and the critical nucleus volume fraction  $\phi_C$  against  $\sigma'^3 / \Delta F_1^3$  according to the simulation results from Fig. 5a, to compare with the linear relationships obtained in Eqs. (8) and (9), as shown in Fig. 5c-d. The predicted straight lines with the slope in Eqs. (8) and (9) are plotted with dotted lines. From Fig. 5c-d, it is clear that the calculated relations of  $\Delta F_C$  against  $\sigma'^3 / \Delta F_1^2$  and  $\phi_C$  against  $\sigma'^3 / \Delta F_1^3$  for the critical nuclei follow straight lines obtained by CNT.

Although eqs. (8) and (9) from the model are slightly rough, the assumptions we make are reasonable. We have changed the adjustment parameter  $\gamma$  of the weight function  $K(\mathbf{r}' - \mathbf{r})$  in eq. (6) to make critical nucleus smoother, which guarantees that the nuclei in different nucleation transitions have same shape. Since we mainly focus on the detailed information of the critical nuclei, whose volume is already large, we consider it always has same macroscopic properties of the final lamellae without influences by the microstructure. In fact, Fig. 2g confirms the interior structure of the critical nucleus is the same as the ultimate object phase, and Fig. 2e confirms the interface between the critical nucleus and the old phase is sharp. Moreover, the deviation between the simulation results and CNT of Fig. 5c becomes smaller with increased  $\chi N$ . Consider our assumptions about the model, the deviation source can be easily revealed. When  $\chi N$  increases, different blocks tend to have a strong segregation. To reduce the interface energy between the nucleus

and the old phase, the interface width becomes narrow and the interface shape tends to be uniform in different transitions, thus the deviation becomes smaller. Look at the case of  $\phi_C$  against  $\sigma'^3 / \Delta F_1^3$ , similar to the former, the simulation results match the predicted line according to eq. (8) well, and the deviation becomes smaller with increased  $\chi N$ . However, the latter deviation is overall slightly large. Except for the reasons above, owing to the limitation of the calculation method, other errors exist when calculating the critical nucleus volume. For example, the adjustment parameter  $\gamma$  in the weight function  $K(\mathbf{r}' - \mathbf{r})$  has a significant influence on the critical nucleus volume, which balances the accuracy of the critical nucleus size and the consistency of shape factors. We believe this method can be applied to the block copolymer nucleation process between various phases under strong segregation, not limited to our case. However, as for other phase transitions under weak  $\chi N$  parameter, the simulation results can be compared with the diffuse interface theory (DIT), in which the interface has a finite thickness instead of a sharp interface in CNT [31,32]. Although DIT is developed based on CNT, it introduces other additional parameters, which makes the model more complicated, and this may be our further research direction.

With the precursor of perforated lamellae is obtained during the phase transition from  $\bar{1}11$  cylinder to (101) lamellae in Fig. 3b, we further study the nucleation transition via the metastable structures. One-step and two-step nucleation pathways are identified in Fig. 6. In the process with one-step nucleation, the final lamellar phase directly nucleates from the cylinder, reaching its only nucleation energy barrier  $\Delta F_C$  ( $\alpha = 0.21$ ). In the other nucleation process, the critical nucleus of

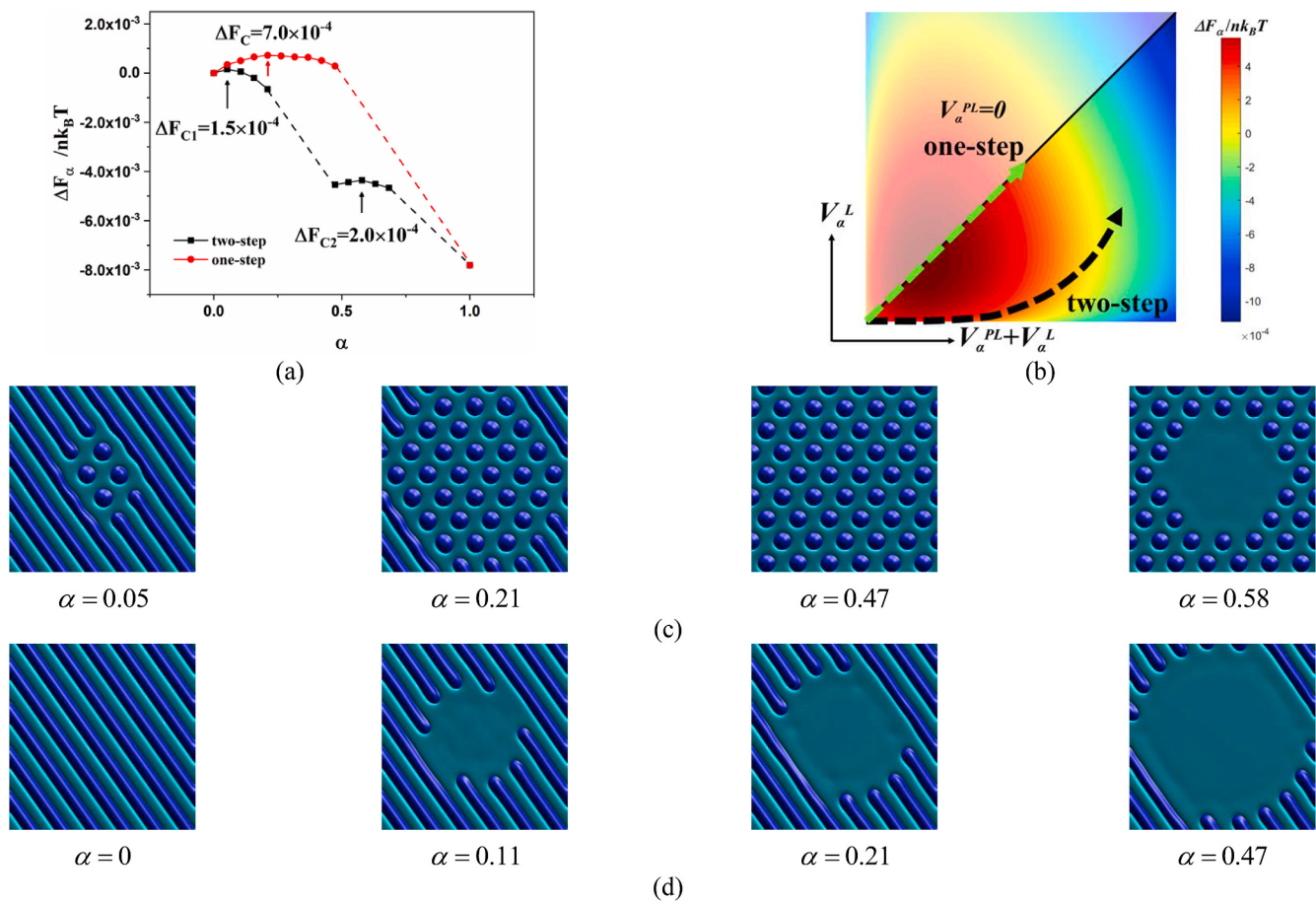


**Fig. 6.** Comparison of one-step and two-step nucleation from  $\bar{1}11$  cylinder to (101) lamellae. (a) MEPs. (b) Contour plot of  $\Delta F(V_\alpha^{PL}, V_\alpha^L)$  as obtained based on the CNT. The black dotted line represents a transition pathway along the two-step nucleation, and the green dotted line represents the transition pathway along the one-step nucleation with  $V_\alpha^{PL} = 0$ . (c) and (d) are the morphology evolution along the (101) plane during two-step and one-step nucleation, respectively. The cyan and blue colors indicate the rods and coils distributions. (For interpretation of the references to color in this figure legend, the reader is referred to the Web version of this article.)

the perforated lamellae appears first ( $\alpha = 0.05$ ). When it slowly extends to the entire cell ( $\alpha = 0.47$ ), the critical nucleus of final phase forms from the perforated lamellae ( $\alpha = 0.58$ ). The critical nuclei formation in the two-step nucleation corresponds to two nucleation energy barriers, namely,  $\Delta F_{C1}$  and  $\Delta F_{C2}$ , both of which are lower than  $\Delta F_C$ . Because the nucleation from cylinder to perforated lamellae has the least nucleation energy barrier, cylinders are most likely to follow the two-step nucleation to the metastable perforated lamellae first, which further validates the appearance of perforated lamellar phase in experiment [59]. The (101) cross-section pictures of the morphologies are shown in Fig. 6c and d. In the two-step process from Fig. 6c, hexagonal hole structure appears with the fusion between independent cylinder phase region along  $\langle\bar{1}\bar{1}1\rangle$  direction, and metastable perforated lamellae forms at the minimum of the energy barrier. Later pores gradually fuse together to form the lamellae nucleus, which is the rate-limiting step with a higher nucleation energy barrier. In the one-step process in Fig. 6d, the lamellae nucleus directly grows along the (101) plane with the fusion between independent cylinder phase region. It needs larger polymer chains transport, leading to higher nucleation energy barrier than the two-step nucleation. The critical nuclei in the two-step nucleation have a smaller volume of  $466.5R_g^3$  and  $1614.2R_g^3$ , however that in the one-step nucleation is larger as  $1962.8R_g^3$ . The detailed comparison between one-step and two-step nucleation is shown in Table 2.

Inspired by work of Kashchiev [60] and Qi [61], we analyse whether the transition from  $\langle\bar{1}\bar{1}1\rangle$  cylinder to (101) lamellae prefers two-step nucleation from the aspect of thermodynamics based on the CNT. Analogously to  $\Delta F(V_a)$  in Eq. (7), we assume that the volume of the nucleus formed by (101) lamellae is  $V_a^L$ , formed by the perforated lamellae is  $V_a^{PL}$ , and  $V_a$  is the total volume of the nucleus during the two-step nucleation, including the nuclei of the metastable and stable phases,  $V_a = V_a^L + V_a^{PL}$ . As the coexistence of two critical nuclei, the energy barrier changes due to three contributions: the difference in bulk free energy between the perforated lamellae and  $\langle\bar{1}\bar{1}1\rangle$  cylinder,  $\Delta F_1^{PL}$ , and that between the (101) lamellae and perforated lamellae,  $\Delta F_1^L$ , where the bulk free energy difference between the cylinder and lamellae is equal to  $\Delta F_1^{PL} + \Delta F_1^L$ ; the unit area of interface energy between the  $\langle\bar{1}\bar{1}1\rangle$  cylinder and the nucleus of perforated lamellae,  $\sigma_{PL}$ , and that between the perforated lamellae and the nucleus of (101) lamellae,  $\sigma_L$ ; the short-range interaction between the two nucleus interfaces, which accounts for the disjoining pressure between them, where  $\Delta\sigma = \sigma - \sigma_{PL} - \sigma_L$  is the spreading parameter and  $\xi$  is the range of interaction [61–63]. The energy barrier changes can then be written as a function of  $V_a^{PL}$  and  $V_a^L$ :

$$\begin{aligned} \Delta F(V_a^{PL}, V_a^L) = & V_a^{PL} \frac{\Delta F_1^{PL}}{V} + \sigma_{PL} (V_a^{PL} + V_a^L)^{2/3} + V_a^L \frac{\Delta F_1^L + \Delta F_1^{PL}}{V} + \sigma_L (V_a^L)^{2/3} \\ & + \Delta\sigma (V_a^{PL} + V_a^L)^{2/3} \exp \left[ - \frac{(V_a^{PL} + V_a^L)^{1/3} - (V_a^L)^{1/3}}{\xi} \right] \end{aligned} \quad (10)$$

Moreover, we can simplify Eq. (10), where the detailed derivation is shown in the Appendix:

**Table 2**

Comparison of Critical Nucleus Information Between One-step and Two-step Nucleation Transitions. (critical nucleus volume fraction  $\phi_C$ , nucleation energy barrier  $\Delta F_C$ , nucleation driving force  $\Delta F_{V,C}$ , interface energy  $\Delta F_{S,C}$ , energy difference between two ends phase  $\Delta F_1$ , and modified unit area of interface energy  $\sigma'$ <sup>a</sup>).

nucleation	$\phi_C$	$\Delta F_C \times 10^{-4}$	$\Delta F_{V,C} \times 10^{-4}$	$\Delta F_{S,C} \times 10^{-4}$	$\Delta F_1 \times 10^{-3}$	$\sigma' \times 10^{-3}$
one-step	0.16	7.0	-13.0	20.0	-7.8	6.7
two-step(step1)	0.04	1.5	-1.7	3.2	-4.5	2.9
two-step(step2)	0.12	2.0	-4.0	6.0	-3.3	2.4

<sup>a</sup> All energy parameters are in the unit of  $nk_B T$ .

$$\begin{aligned} \Delta F(V_a^{PL}, V_a^L) = & \phi_a \Delta F_1^{PL} + \sigma'_{PL} (\phi_a)^{2/3} + \phi_a^L \Delta F_1^L + \sigma'_L (\phi_a^L)^{2/3} \\ & + \Delta\sigma' (\phi_a)^{2/3} \exp \left[ - \frac{(V_a)^{1/3} - (V_a^L)^{1/3}}{\xi} \right] \end{aligned} \quad (11)$$

where  $\sigma'_{PL}$  is the modified result of  $\sigma_{PL}$ ,  $\sigma'_{PL} = (V\Delta F_{C1} - V_C^{PL}\Delta F_1^{PL}) / [(V_C^{PL})^{2/3}L]$ , and  $\sigma'_L$  has same definition as  $\sigma'_L = (V\Delta F_{C2} - V_C^L\Delta F_1^L) / [(V_C^L)^{2/3}L]$ .  $V_C^{PL}$  and  $V_C^L$  represent the critical nucleus volume of perforated lamellae and (101) lamellae.  $\phi_a$  is the nucleus volume fraction containing two nuclei,  $\phi_a = (V_a^{PL} + V_a^L)/V$ , and  $\phi_a^L$  is the nucleus volume fraction of (101) lamellae,  $\phi_a^L = V_a^L/V$ . The adjustable parameter  $\xi$  of the third term in the right-hand side is set as 1, and the modified spreading parameter  $\Delta\sigma' = \sigma' - \sigma'_{PL} - \sigma'_L$ . All parameters are shown in Table 2.

The contour plot of  $\Delta F(V_a^{PL}, V_a^L)$  from Eq. (11) is illustrated schematically in Fig. 6b. The free energy landscape shows that a high energy barrier stands between  $\langle\bar{1}\bar{1}1\rangle$  cylinder and (101) lamellae with the energy costs caused by the interface between them, where the nucleation proceeds along the diagonal at  $V_a^{PL} = 0$ . This prevents direct nucleation from  $\langle\bar{1}\bar{1}1\rangle$  cylinder to (101) lamellae. Instead, a lower energy barrier path involves the formation of the perforated lamellae nucleus, which beyond the critical energy point grows spontaneously into the metastable perforated lamellae. A ridge on the free energy landscape separates two free energy basins associated with the (101) lamellae and the perforated lamellae. The nucleation transition along the roundabout pathway (the black dotted line) is what leads to a well-manifested two-step nucleation, where a perforated lamellae first forms and grows before the (101) lamellae nucleates, yielding two separate energy barriers. However, it is worth noting that the nucleus of (101) lamellae can grow inside the perforated lamellae nucleus with a smallest energy barrier when  $V_a^{PL}$  reaches its maximum, which explains the morphologies obtained in Fig. 6c that the critical nucleus of the final phase does not form until the perforated lamellae extends to the entire cell.

#### 4. Conclusion

Combine the string method and SCFT, we study the nucleation transition of rod-coil block copolymer by extending the calculation size to 216 times the initial cell size in 3D. For the first time, we systematically investigate the nucleation transitions from  $[111]$ ,  $\langle\bar{1}\bar{1}1\rangle$  cylinders to (101) lamellae with chain rigidity. The results reveal that different directions of initial cylinders can lead to different nucleation pathways. The nucleation from cylinder with  $\langle\bar{1}\bar{1}1\rangle$  direction has a minimal nucleation energy barrier, which is mainly due to the lower interface energy determined within the CNT. Importantly, our method gives the specific morphologies of the critical nuclei. The interior structure of the critical nucleus is the same as the ultimate object phase, and the interface between rods and coils is sharp. Compared with  $\langle\bar{1}\bar{1}1\rangle$  cylinder,  $[111]$  cylinder has an inconsistent direction with (101) lamellae, and it needs long transition path and multi-step reorientations to nucleate. These two factors directly lead to the higher interface energy with a rough and large critical nucleus.

In addition, nucleation under different Flory-Huggins interactions and nucleation via a metastable phase are presented. The simulation results agree with the prediction of CNT. First, the relations of the  $\Delta F_C$  vs.  $\sigma'^3/\Delta F_1^2$  and  $\phi_C$  vs.  $\sigma'^3/\Delta F_1^3$  follow straight lines as deduced in Eqs. (8) and (9). Second, the two-step nucleation shows a lower energy barrier path consistent with the free energy landscape calculated based on CNT. This work does not require prior knowledge of the nucleation transition pathway, and it is applicable to the complicated rod-coil block copolymers.

## CRediT authorship contribution statement

**Jingyu Shao:** Methodology, Software, Validation, Formal analysis, Investigation, Data curation, Writing - original draft. **Yuliang Yang:** Supervision. **Ping Tang:** Conceptualization, Resources, Writing - review & editing, Project administration, Funding acquisition.

## Declaration of competing interest

The authors declare that they have no known competing financial

## Appendix

Since our model has a consistent unit volume of nucleation driving force and a sharp interface between nucleus and mother phase, we can obtain the change of the energy barrier:

$$\Delta F(V_a) = F(V_a) - F_0 = V_a \frac{\Delta F_1}{V} + \sigma(V_a)^{2/3} \quad (12)$$

where we take the “interface energy density”  $\sigma$  as a fitting parameter for the nucleation energy barrier, and several prefactors such as shape factors of the critical nucleus have been included into  $\sigma$ :

$$\sigma = \frac{\Delta F_C - V_C \Delta F_1 / V}{V_C^{2/3}} \quad (13)$$

Substituting  $\sigma$  into Eq. (12), and we can obtain Eq. (7) as:

$$\begin{aligned} \Delta F(V_a) &= V_a \frac{\Delta F_1}{V} + \frac{\Delta F_C - V_C \Delta F_1 / V}{V_C^{2/3}} V_a^{2/3} \\ &= \phi_a \Delta F_1 + \frac{V \Delta F_C - V_C \Delta F_1}{V_C^{2/3} L} \phi_a^{2/3} \\ &= \phi_a \Delta F_1 + \sigma' \phi_a^{2/3} \end{aligned} \quad (14)$$

where the modified unit area of interface energy  $\sigma'$  equals to  $(V \Delta F_C - V_C \Delta F_1) / (V_C^{2/3} L)$ .

We can simplify Eq. (10) by replacing  $V_a^{PL}$  with  $V_a$ , where  $V_a^{PL} = V_a - V_a^L$ :

$$\begin{aligned} \Delta F(V_a^{PL}, V_a^L) &= V_a \frac{\Delta F_1^{PL}}{V} + \sigma_{PL}(V_a)^{2/3} + V_a^L \frac{\Delta F_1^L}{V} + \sigma_L(V_a^L)^{2/3} \\ &\quad + \Delta \sigma(V_a)^{2/3} \exp \left[ -\frac{(V_a)^{1/3} - (V_a^L)^{1/3}}{\xi} \right] \end{aligned} \quad (15)$$

Following the derivation above, we take each “interface energy density” in Eq. (15) as the fitting parameter for the corresponding nucleation energy barrier in the two-step nucleation:

$$\sigma_{PL} = \frac{\Delta F_{C1} - V_C^{PL} \Delta F_1^{PL} / V}{(V_C^{PL})^{2/3}} \quad (16)$$

$$\sigma_L = \frac{\Delta F_{C2} - V_C^L \Delta F_1^L / V}{(V_C^L)^{2/3}} \quad (17)$$

Substituting Eqs. (16) and (17) into Eq. (15), and replace the nucleus volume with the nucleus volume fraction, we obtain:

$$\begin{aligned} \Delta F(V_a^{PL}, V_a^L) &= \phi_a \Delta F_1^{PL} + \sigma'_{PL}(\phi_a)^{2/3} + \phi_a^L \Delta F_1^L + \sigma'_L(\phi_a^L)^{2/3} \\ &\quad + \Delta \sigma'(\phi_a)^{2/3} \exp \left[ -\frac{(V_a)^{1/3} - (V_a^L)^{1/3}}{\xi} \right] \end{aligned} \quad (18)$$

where the modified results of Eq. (16) and Eq. (17) are obtained as:

$$\sigma'_{PL} = (V \Delta F_{C1} - V_C^{PL} \Delta F_1^{PL}) / [(V_C^{PL})^{2/3} L] \quad (19)$$

$$\sigma'_L = (V \Delta F_{C2} - V_C^L \Delta F_1^L) / [(V_C^L)^{2/3} L] \quad (20)$$

## References

- [1] D. Kashchiev, Nucleation: Basic Theory with Applications, Elsevier, 2000.
- [2] K. Kelton, A.L. Greer, Nucleation in Condensed Matter: Applications in Materials and Biology, Elsevier, 2010.
- [3] Y. Shibuta, S. Sakane, E. Miyoshi, S. Okita, T. Takaki, M. Ohno, Heterogeneity in homogeneous nucleation from billion-atom molecular dynamics simulation of solidification of pure metal, *Nat. Commun.* 8 (2017) 9.
- [4] C.Q. Yuan, A. Levin, W. Chen, R.R. Xing, Q.L. Zou, T.W. Herling, P.K. Challa, T.P. J. Knowles, X.H. Yan, Nucleation and growth of amino acid and peptide supramolecular polymers through liquid-liquid phase separation, *Angew. Chem. Int. Ed.* 58 (2019) 18116–18123.
- [5] J.W. Gibbs, On the equilibrium of heterogeneous substances, *Trans. Conn. Acad. Arts Sci. III* (1878) 108–524.
- [6] J.W. Gibbs, A method of geometrical representation of the thermodynamic properties by means of surfaces, *Trans. Conn. Acad. Arts Sci. II* (1873) 382–404.
- [7] M. Volmer, Nucleus formation in supersaturated systems, *Z. Phys. Chem.* 119 (1926) 277–301.
- [8] R. Becker, W. Doring, Kinetic treatment of germ formation in supersaturated vapour, *Ann. Phys.* 24 (8) (1935) 719–752.
- [9] C.M. Bates, F.S. Bates, 50th anniversary perspective: block polymers-pure potential, *Macromolecules* 50 (1) (2017) 3–22.
- [10] F.S. Bates, G.H. Fredrickson, Block copolymer thermodynamics: theory and experiment, *Annu. Rev. Phys. Chem.* 41 (1) (1990) 525–557.
- [11] M.W. Matsen, M. Schick, Stable and unstable phases of a diblock copolymer melts, *Phys. Rev. Lett.* 72 (1994) 2660.
- [12] F. Drolet, G.H. Fredrickson, Combinatorial screening of complex block copolymer assembly with self-consistent field theory, *Phys. Rev. Lett.* 83 (21) (1999) 4317–4320.
- [13] E.B. Zhulina, S.S. Sheiko, A.V. Dobrynin, O.V. Borisov, Microphase segregation in the melts of bottlebrush block copolymers, *Macromolecules* 53 (7) (2020) 2582–2593.
- [14] N. Hampu, M.A. Hillmyer, Molecular engineering of nanostructures in disordered block polymers, *ACS Macro Lett.* 9 (3) (2020) 382–388.
- [15] D.W. Sun, M. Muller, Process-accessible states of block copolymers, *Phys. Rev. Lett.* 118 (6) (2017) 6.
- [16] S. Sakurai, H. Umeda, C. Furukawa, H. Irie, S. Nomura, H.H. Lee, J.K. Kim, Thermally induced morphological transition from lamella to gyroid in a binary blend of diblock copolymers, *J. Chem. Phys.* 108 (10) (1998) 4333–4339.
- [17] D.A. Hajduk, H. Takenouchi, M.A. Hillmyer, F.S. Bates, M.E. Vigild, K. Almdal, Stability of the perforated layer (pl) phase in diblock copolymer melts, *Macromolecules* 30 (13) (1997) 3788–3795.
- [18] M. Imai, K. Sakai, M. Kikuchi, K. Nakaya, A. Saeki, T. Teramoto, Kinetic pathway to double-gyroid structure, *J. Chem. Phys.* 122 (21) (2005) 10.
- [19] M. Brinkmann, N. Charoenthai, R. Traiphob, P. Piyakulawat, J. Wlosnewski, U. Asawapirom, Structure and morphology in highly oriented films of poly(9,9-bis(n-octyl)fluorene-2,7-diyl) and poly(9,9-bis(2-ethylhexyl)fluorene-2,7-diyl) grown on friction transferred poly(tetrafluoroethylene), *Macromolecules* 42 (21) (2009) 8298–8306.
- [20] M. Brinkmann, Structure and morphology control in thin films of regioregular poly(3-hexylthiophene), *J. Polym. Sci., Part B: Polym. Phys.* 49 (17) (2011) 1218–1233.
- [21] K. Cui, Z. Ma, N. Tian, F. Su, D. Liu, L. Li, Multiscale and multistep ordering of flow-induced nucleation of polymers, *Chem. Rev.* 118 (4) (2018) 1840–1886.
- [22] R.S. Graham, Understanding flow-induced crystallization in polymers: a perspective on the role of molecular simulations, *J. Rheol.* 63 (1) (2019) 203–214.
- [23] W. Hu, D. Frenkel, V.B.F. Mathot, Simulation of shish-kebab crystallite induced by a single prealigned macromolecule, *Macromolecules* 35 (19) (2002) 7172–7174.
- [24] T. Philippe, Nucleation and interfacial adsorption in ternary systems, *J. Chem. Phys.* 142 (9) (2015), 094501.
- [25] X. Cheng, L. Lin, E. Weinan, P. Zhang, A.-C. Shi, Nucleation of ordered phases in block copolymers, *Phys. Rev. Lett.* 104 (14) (2010) 148301.
- [26] N. Ji, P. Tang, F. Qiu, Kinetic pathways of lamellae to gyroid transition in weakly segregated diblock copolymers, *Macromolecules* 48 (23) (2015) 8681–8693.
- [27] J.D. Hoffman, R.L. Miller, Kinetic of crystallization from the melt and chain folding in polyethylene fractions revisited: theory and experiment, *Polymer* 38 (13) (1997) 3151–3212.
- [28] P.D. Olmsted, W.C.K. Poon, T.C.B. McLeish, N.J. Terrill, A.J. Ryan, Spinodal-assisted crystallization in polymer melts, *Phys. Rev. Lett.* 81 (2) (1998) 373–376.
- [29] G. Strobl, From the melt via mesomorphic and granular crystalline layers to lamellar crystallites: a major route followed in polymer crystallization? *Eur. Phys. J. E* 3 (2) (2000) 165–183.
- [30] J. Yu, F. Liu, P. Tang, F. Qiu, H. Zhang, Y. Yang, Effect of geometrical asymmetry on the phase behavior of rod-coil diblock copolymers, *Polymers* 8 (5) (2016) 184.
- [31] L. Granasy, Diffuse interface theory of nucleation, *J. Non-Cryst. Solids* 162 (3) (1993) 301–303.
- [32] L. Granasy, Fundamentals of the diffuse interface theory of nucleation, *J. Phys. Chem.* 100 (25) (1996) 10768–10770.
- [33] F. Spaepen, Homogeneous nucleation and the temperature dependence of the crystal-melt interfacial tension, in: H. Ehrenreich, D. Turnbull (Eds.), *Solid State Physics - Advances in Research and Applications*, 47, 1994, pp. 1–32.
- [34] G. Bai, D. Gao, Z. Liu, X. Zhou, J. Wang, Probing the critical nucleus size for ice formation with graphene oxide nanosheets, *Nature* 576 (7787) (2019) 437–441.
- [35] R.A. Wickham, A.C. Shi, Z.G. Wang, Nucleation of stable cylinders from a metastable lamellar phase in a diblock copolymer melt, *J. Chem. Phys.* 118 (22) (2003) 10293–10305.
- [36] V. Pryamitsyn, V. Ganesan, Self-assembly of rod-coil block copolymers, *J. Chem. Phys.* 120 (12) (2004) 5824–5838.
- [37] P. Tang, F. Qiu, H.D. Zhang, Y.L. Yang, Phase separation patterns for diblock copolymers on spherical surfaces: a finite volume method, *Phys. Rev. E* 72 (1) (2005).
- [38] G. Fredrickson, *The Equilibrium Theory of Inhomogeneous Polymers*, Oxford University Press on Demand, 2006.
- [39] G. Tzeremes, K.O. Rasmussen, T. Lookman, A. Saxena, Efficient computation of the structural phase behavior of block copolymers, *Phys. Rev. E* 65 (4) (2002), 041806.
- [40] Y.A. Krikis, P.G. Khalatur, Parallel algorithm for 3d scf simulation of copolymers with flexible and rigid blocks, *Macromol. Theory Simul.* 21 (6) (2012) 382–399.
- [41] G. Yang, P. Tang, Y. Yang, Q. Wang, Self-assembled microstructures of confined rod-coil diblock copolymers by self-consistent field theory, *J. Phys. Chem. B* 114 (46) (2010) 14897–14906.
- [42] J. Gao, P. Tang, Y. Yang, Non-lamellae structures of coil-semiflexible diblock copolymers, *Soft Matter* 9 (1) (2013) 69–81.
- [43] W. E, W. Ren, E. Vanden-Eijnden, String method for the study of rare events, *Phys. Rev. B* 66 (5) (2002), 052301.
- [44] W. Ren, Higher order string method for finding minimum energy paths, *Commun. Math. Sci.* 1 (2) (2003) 377–384.
- [45] W. E, W. Ren, E. Vanden-Eijnden, Energy landscape and thermally activated switching of submicron-sized ferromagnetic elements, *J. Appl. Phys.* 93 (4) (2003) 2275–2282.
- [46] T.J. Sun, F.Q. Liu, P. Tang, F. Qiu, Y.L. Yang, Construction of rod-forming single network mesophases in rod-coil diblock copolymers via inversely designed phase transition pathways, *Macromolecules* 51 (15) (2018) 5773–5787.
- [47] L. Lin, X. Cheng, W. E, A.-C. Shi, P. Zhang, A numerical method for the study of nucleation of ordered phases, *J. Comput. Phys.* 229 (5) (2010) 1797–1809.
- [48] K. Jiang, C. Wang, Y.Q. Huang, P.W. Zhang, Discovery of new metastable patterns in diblock copolymers, *Commun. Comput. Phys.* 14 (2) (2013) 443–460.
- [49] M.W. Matsen, Cylinder <-> gyroid epitaxial transitions in complex polymeric liquids, *Phys. Rev. Lett.* 80 (20) (1998) 4470–4473.
- [50] M.W. Matsen, Cylinder <-> sphere epitaxial transitions in block copolymer melts, *J. Chem. Phys.* 114 (18) (2001) 8165–8173.
- [51] A. Gulyieva, M. Vayer, F. Warmornt, A. Takano, Y. Matsushita, C. Sinturel, Transition pathway between gyroid and cylindrical morphology in linear triblock terpolymer thin films, *Macromolecules* 52 (17) (2019) 6641–6648.
- [52] N.W. Ashcroft, N.D. Mermin, *Solid State Physics*, Holt, 1976.
- [53] A. Arora, J. Qin, D.C. Morse, K.T. Delaney, G.H. Fredrickson, F.S. Bates, K. D. Dorfman, Broadly accessible self-consistent field theory for block polymer materials discovery, *Macromolecules* 49 (13) (2016) 4675–4690.
- [54] J. Shao, N. Jiang, H. Zhang, Y. Yang, P. Tang, Target-directed design of phase transition path for complex structures of rod-coil block copolymers, *ACS Omega* 4 (23) (2019) 20367–20380.
- [55] B. McCulloch, G. Portale, W. Bras, J.A. Pople, A. Hexemer, R.A. Segalman, Dynamics of magnetic alignment in rod-coil block copolymers, *Macromolecules* 46 (11) (2013) 4462–4471.
- [56] R. Holyst, P. Oswald, Liquid-crystalline order in polymer systems: basic models, *Macromol. Theory Simul.* 10 (1) (2001) 1–16.
- [57] B.D. Olsen, M. Shah, V. Ganesan, R.A. Segalman, Universalization of the phase diagram for a model rod-coil diblock copolymer, *Macromolecules* 41 (18) (2008) 6809–6817.
- [58] P.J. Flory, *Principles of Polymer Chemistry*, 1953. Ithaca, New York.
- [59] I.W. Hamley, K.A. Koppi, J.H. Rosedale, F.S. Bates, K. Almdal, K. Mortensen, Hexagonal mesophases between lamellae and cylinders in a diblock copolymer melt, *Macromolecules* 26 (22) (1993) 5959–5970.
- [60] D. Kashchiev, Classical nucleation theory approach to two-step nucleation of crystals, *J. Cryst. Growth* 530 (2020) 13.
- [61] W. Qi, Y. Peng, Y. Han, R.K. Bowles, M. Dijkstra, Nonclassical nucleation in a solid-solid transition of confined hard spheres, *Phys. Rev. Lett.* 115 (18) (2015) 185701.
- [62] A.K. Shchekin, I.V. Shabaev, A.I. Rusanov, Thermodynamics of droplet formation around a soluble condensation nucleus in the atmosphere of a solvent vapor, *J. Chem. Phys.* 129 (21) (2008) 214111.
- [63] M. Iwamatsu, Free-energy landscape of nucleation with an intermediate metastable phase studied using capillarity approximation, *J. Chem. Phys.* 134 (16) (2011) 164508.